Type of the Paper (Article)

Drone-based hyperspectral and thermal imagery for quantifying upland rice growth and water use efficiency after biochar application

Hongxiao Jin [1,10,*], Christian Josef Köppl [1], Benjamin M. C. Fischer [2,3], Johanna Rojas-Conejo [4], Mark S. Johnson [5], Laura Morillas [6], Steve W. Lyon [2,9], Ana M. Durán-Quesada [7,8], Andrea Suárez-Serrano [4], Stefano Manzoni [2] and Monica Garcia [1]

1 Department of Environmental Engineering, Technical University of Denmark, Denmark; mgarc@env.dtu.dk; chkop@env.dtu.dk
2 Department of Physical Geography and Bolin Centre for Climate Research, Stockholm University, Stockholm, Sweden; benjamin.fischer@natgeo.su.se; stefano.manzoni@natgeo.su.se; steve.lyon@su.se
3 Department of Earth Sciences, Uppsala University, Sweden;
4 Water Resources Center for Central America and the Caribbean (HIDROCEC). Universidad Nacional de Costa Rica. Liberia. Costa Rica; johanna.rojas.conejo@una.ac.cr; andrea.suarez.serrano@una.cr
5 Department of Earth, Ocean and Atmospheric Sciences, University of British Columbia, Canada; mark.johnson@ubc.ca
6 Centre for Sustainable Food Systems, University of British Columbia, Canada; laura.morillas@ubc.ca
7 Atmospheric, Oceanic and Planetary Physics Department & Climate System Observation Laboratory, School of Physics, University of Costa Rica, Costa Rica; ANA.DURANQUESADA@ucr.ac.cr
8 Center for Geophysical Research, University of Costa Rica, Costa Rica;
9 School of Environment and Natural Resources, Ohio State University, USA
10 Sino-Danish Center for Education and Research (SDC), Denmark
* Correspondence: honji@env.dtu.dk; Tel.: +45 6085 58 78

Abstract: Low-cost miniature hyperspectral and thermal cameras onboard lightweight unmanned aerial vehicles (UAV) bring new opportunities for monitoring land surface variables at unprecedented fine spatial resolution with acceptable accuracy. This research applies hyperspectral and thermal imagery from a drone to quantify upland rice growth and water use efficiency (WUE) after biochar application in a Costa Rican dry region. The field flights were conducted over two experimental groups with bamboo biochar and sugarcane biochar amendments and one control group without biochar application. Rice canopy biophysical variables were estimated by inversion of a canopy radiative transfer model on hyperspectral reflectance. Variations in gross primary production (GPP) and WUE across treatments were estimated from the normalized difference vegetation index (NDVI), canopy chlorophyll content (CCC), and evapotranspiration. We found that GPP was increased by 41.9±3.4 % when using bamboo biochar and 17.5±3.4 % when using sugarcane biochar, which was probably due to higher soil moisture in the biochar-amended plots and led to significantly higher WUE by 40.8±3.5 % in bamboo biochar and 13.4±3.5 % in sugarcane biochar. This study demonstrated the use of hyperspectral and thermal imagery from drone to provide indicators for quantifying biochar effects on tropical dry cropland by integrating with ground point samples and physical models.

Keywords: Unmanned aerial vehicle (UAV); hyperspectral and thermal imagery; gross primary production (GPP); water use efficiency (WUE); biochar

1. Introduction

Land surface variables are required for land surface modeling of carbon, water, and energy processes. A low-cost miniature hyperspectral and thermal cameras onboard lightweighted unmanned aerial vehicle (UAV) are promising to provide spatially explicit land surface variables and as an efficient tool supporting precision farming and crops management [e.g. 1,2,3]. Infrared thermography has been used to diagnose crop water deficit and

Preprints (www.preprints.org) | NOT PEER-REVIEWED | Posted: 9 April 2021 doi:10.20944/preprints202104.0267.v1

drought stress [4-6]. A miniature hyperspectral camera onboard a UAV with dozens or even 100+ continuous narrow bands with high spectral resolution is promising for formulating different vegetation indices to evaluate crop growth and retrieving crop biophysical variables for precision agriculture [7].

Due to its simplicity, vegetation indices are often used to estimate a certain land surface variable with spectral band combinations. For example, the normalized difference vegetation index (NDVI) formulated using red and near-infrared bands is widely used to indicate land surface greenness [8], and narrow hyperspectral band combinations for leaf chlorophyll estimation [9]. Recently machine learning techniques are increasingly used to estimate land surface variables based on large field measurements, for example, partial least squared regression [10], artificial neural network [11], and random forest [12]. These empirical methods need site-specific land surface variables for model training and the trained model may not be suitable for other sites. A radiative transfer model, such as PRO4SAIL [13], can simulate hyperspectral reflectance close to the field measured reflectance with optimal inputs. The inverse of the radiative transfer model based on field hyperspectral measurement can obtain optimized input variables by minimizing the difference between the modelled and the measured reflectance. Such a physically-based model do not need field-measured land surface variables in model optimization process, and can be used to general situations with field hyperspectral reflectance measurements.

Biochar is an old technique used for soil amendment in the Amazon region centuries ago [14,15]. The porous charcoal has a large surface area that can bind and retain soil water, nutrients, minerals, and reduce nutrient leaching and volatilizing loss that helps to increase long-term plant water availability and soil fertility [16,17]. Charcoal itself is decomposition-resistant, contributing to soil carbon sequestration and atmospheric carbon reduction [18]. Biochar as a soil amendment is thus considered valuable to increase crop production and resilience to drought [17], and meanwhile, a negative-emission strategy to mitigate climate change [15].

As the implementation of biochar is to incorporate good agricultural practices, more study is needed to better understand its effects on crop growth, soil water status and usage, and land surface energy balance. Using a conceptual model, Fischer et al. [17] showed that biochar amendment—by shifting the soil water retention curve—should increase soil water availability under water-limited conditions. As a result, the long-term mean evapotranspiration (ET) rate is expected to increase after biochar amendment, which in turn should increase the gross primary production (GPP) due to the joint regulation of transpiration and photosynthesis by stomata. However, the impacts on plant water use efficiency (WUE=GPP/ET, the rate of GPP per unit water consumption) are not clear. Moreover, the ET is not always increased in biochar-amended fields, in contrast to model predictions [17].

These divergent effects of biochar on crop growth and soil hydraulic properties highlight our limited understanding of the effects of biochar on crop production and soil water usage [17,19-21]. The apparent gap between the theory and empirical evidence on biochar effects may be also due to extrapolating documented biochar effects on soil properties from discrete *in situ* point measurements to the field or farm scale. Furthermore, as there are concurrent impacts of biochar on soil and plant properties, synthesizing them by combining both spatial and point measurements may provide a broader picture of crop responses after biochar application.

This study explores the potentials of UAV-based hyperspectral and thermal sensing for a spatially improved understanding of the functioning of biochar in tropical dryland. We investigate the effect of biochar in a field experiment with upland rice (*Oryza sativa* L.) in the North Pacific of Costa Rica to assess changes associated with energy, water, and carbon fluxes such as GPP, soil water availability, ET, and WUE using hyperspectral and thermal imaging technology onboard a hexacopter. *In situ* and laboratory measurements on soil and rice plants were made during a four-day field campaign. Combining the UAV-derived land surface and biophysical variables, measurements, and models, the study

Preprints (www.preprints.org) | NOT PEER-REVIEWED | Posted: 9 April 2021 doi:10.20944/preprints202104.0267.v1

aims to assess dryland crop and soil water responses after biochar application, while testing the applicability of hyperspectral and thermal imagery in support of agricultural management.

2. Materials and Methods

2.1. Biochar experiment plots

The experiment was conducted on an about 8 m × 20 m site parcel, located at the Enrique Jiménez Núñez Experimental Station in Costa Rica (10.3436°N, 85.1353° W; 17 m asl, Figure 1). The North Pacific of Costa Rica is a drought-prone region, in which severe dry events are mostly related to the warm phase of the El Niño-Southern Oscillation phenomenon [22,23]. The region features increasing aridity and rainfall reduction trends, which have been projected to exacerbate along with global warming, threatening both water resources availability and agricultural activities [22,24]. In the long-term, the region is characterized as a tropical savannah climate with a marked dry season from mid-November to April. The long-term mean annual rainfall is about 1547 mm/yr and the mean annual temperature 27.4 °C (100-year period). The soil at the experimental site has a clay loam texture. The experiment consisted of three groups in triplicate separated by 0.8 m wide corridors. Due to logistic reasons, the experimental plots were set in a fairly small area, neglecting all other nuisance environmental factors without using a randomized block design. Two treatment groups used local Guadua bamboo (*Guadua angustifolia*) biochar (BC1) and Taiwan sugarcane (*Saccharum officinarum*) filter cake biochar (BC2) respectively, and the control group (C) had no biochar addition. Upland rice seeds (variety Palmar 18) were sown on July 18, 2018, irrigated and fertilized to encourage germination and seedling growth following the common local farming practice. Harvest took place on 21 November 2018 and indicated the end of the experiment. See [25] for details of biochar experimental design.

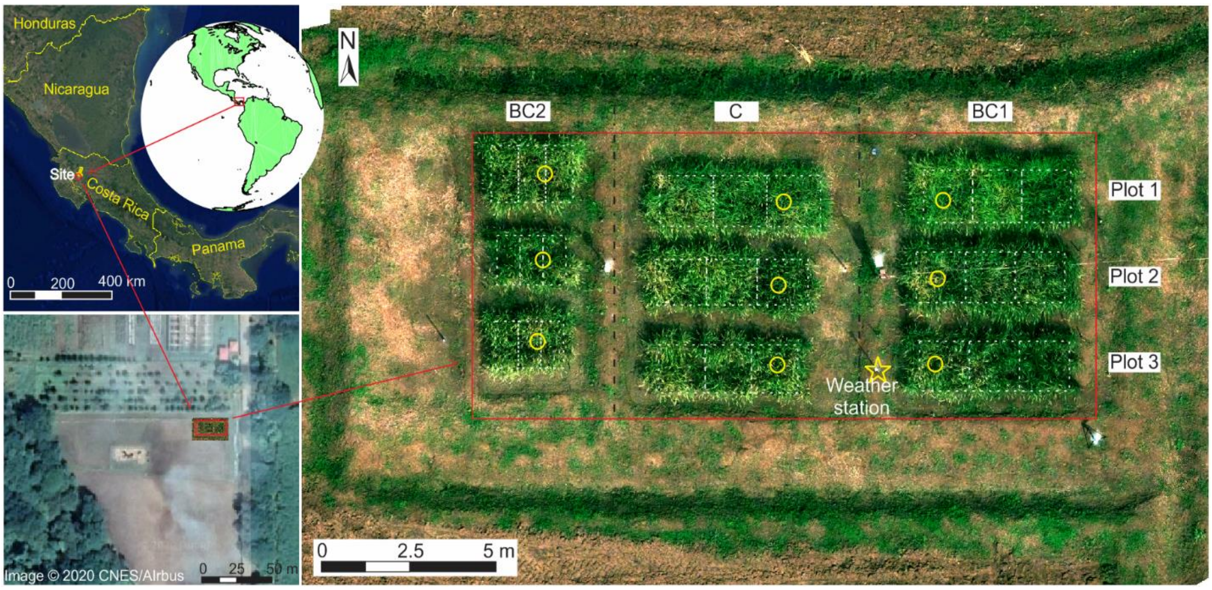

Figure 1. Location of biochar plots at an upland rice experimental site in Costa Rica. The experiment consisted of three groups (BC1, BC2, and C) in triplicate (Plot 1, 2, and 3). Each plot was divided into 3 sub-plots used in statistical analysis (indicated as dashed lines). The true-color image (4.5 mm resolution) is from a Cubert FireflEYE 185 VNIR camera (band 56, 29, and 12) taken on November 14, 2018, orthorectified and mosaicked using Agisoft Metashape software. The star (☆) denotes the location of the weather station, and circles (○) the locations of soil sensors.

2.2. UAV field campaign

The UAV field campaign was carried out using a hexacopter (DJI M600 Pro, Dajiang, China) on November 14, 16, 19, and 21, 2018 before harvest. The hexacopter has a payload capacity of 6 kg and a flight time of 35 minutes under minimal payload. In the campaign, the UAV was flying at a height of about 30 m above the ground. The UAV position was recorded by the three sets of GNSS and IMU systems inbuilt with the drone. A gimbal (Gremsy T7, Gremsy, Viet Nam) was used to enable the camera to consistently viewing the nadir direction. We used a hyperspectral camera (FireflEYE 185ST, Cubert, Germany) and a thermal camera (324×256 Pixels, Tau2 324, FLIR, USA) with the attained ground resolutions of 4.5 mm and 2.25 cm respectively to investigate the plant production, soil, and surface properties. The Cubert hyperspectral camera has 50×50 pixels, with each pixel spanning from 450 to 950 nm in 138 wavebands. The camera has an extra panchromatic band of 1000×1000 pixels to facilitate sharpening the hyperspectral bands. It has been shown that the best spatial and spectral accuracy can be achieved from Cubert panchromatic sharpening at a flying height of 30 m [26]. During the flight, a spectrometer (Flame S VIS-NIR, Ocean Optics, USA) was mounted on the drone to simultaneously collect spectral irradiance.

2.3. Ground measurements

Hyperspectral reflectance signatures of rice canopy and soil background were measured respectively using a spectroradiometer (FieldSpec HandHeld 2, ASD, USA) and a white Spectralon reference panel (Labsphere, USA). Canopy reflectance was measured on each plot three times. The average spectral reflectance was used to verify Cubert hyperspectral camera measurements.

The leaf gravimetric water content was measured using a destructive method. Three samples of whole rice leave (including leaf blade and sheath, and the stem under the sheath) were taken in each plot on November 19, 2018. Each sample was weighed fresh, cut into small pieces, and heated in an oven at 70 °C for 24 hours in a laboratory. The leaf water mass was determined as the difference between the fresh and the dry leaf mass. The leaf gravimetric water content was defined as the ratio of leaf water mass to fresh mass [g/g]. Leaf nutrient content was also determined in the laboratory using the total digestion method on leaf samples. The macro-elements of nitrogen (N), phosphorous (P), and potassium (K) concentration are determined as a percentage (%) of the dry matter. One soil sample was collected from each plot. The total nitrogen concentration in each sample was tested using a CN 628 Dumas analyzer (LECO, US) in the laboratory in National Agricultural Technology Institute (INTA), Costa Rica.

An automatic meteorological station (Vaisala WT520, Waisala, Finland) was installed at a height of 1.5 m above the ground to continuously monitor precipitation, wind speed and direction, air temperature, relative humidity, and atmospheric pressure (Figure 1). Each plot was instrumented with two in situ sensors at 15 cm below the surface (Figure 1), including one sensor (Decagon GS3, METER Group, USA) measuring volumetric soil water content, soil electrical conductivity, and soil temperature, and another sensor (Decagon MPS6, METER Group, USA) measuring soil matric potential and soil temperature. The sensors were connected to a data logger (CR1000, Campbell Scientific, USA) to collect the data at 30-minute intervals from 18 July to 21 November 2018.

2.4. Data processing

2.4.1 Radiometric correction: Digital Number (DN) to physical values

The DN values of pan-sharpened high-resolution hyperspectral image were transformed to absolute radiance [W/m²/nm/sr] values using per-band per-pixel sensitivity factors that were determined in a photonics laboratory of the Technical University of Denmark before the campaign. The spectral irradiance [W/m²/nm] measured by the on-flight spectrometer was converted to per-band per-pixel irradiance value for the Cubert camera using the spectral response function of each pixel that was determined in the same laboratory. The reflectance of each pixel was calculated as:

$$\rho = \pi \frac{radiance}{irradiance}, \tag{1}$$

The brightness temperature was calculated using calibration parameters and the inverse of Planck's Law following Köppl [27]:

$$T_b = \log^{-1}\left(\frac{k_1}{DN+k_2+k_3T_c}+1\right), \tag{2}$$

where k_1, k_2, and k_3 are calibration parameters, DN is the digital number of FLIR camera images, and Tc is the camera detector core temperature.

2.4.2 Image Orthorectification and mosaicking

After transforming all the images into hyperspectral reflectance and land surface temperature, the Agisoft Metashape software (Agisoft, Russia) was used to generate an orthorectified and mosaicked (orthomosaic) image that covering the whole experiment rice field. To avoid processing of large volume of hyperspectral data, the camera locations and digital elevation model (DEM) were estimated from the panchromatic gray images only, and then the orthomosaic hyperspectral image was generated from the camera locations and the DEM that were estimated from the Cubert gray images. The DEM was also used to estimate rice canopy heights by subtracting the average surrounding soil background elevation from the canopy elevation.

2.4.3 NDVI and Variations in gross primary production (GPP)

The orthomosaic hyperspectral reflectance values were corrected using an empirical line correction method by selecting two pseudo-invariant features in the scene: an unshaded fixed white instrument box and a patch of dark bare soil that were identified from the composite true-color hyperspectral images. Then the leaf area index (LAI, [-]) and canopy chlorophyll content (CCC, [g/m^2 ground area]) were estimated using the inversion of PRO4SAIL Model (available at http://teledetection. ipgp.jussieu.fr/prosail/) with the corrected hyperspectral reflectance, pixel by pixel at 2.25 cm resolution (resampled from 4.5 mm to match thermal images). The NDVI was calculated using Band 104 (NIR) and Band 56 (red): NDVI = (NIR-red)/(NIR+red). The NDVI has been shown to have a linear relationship with the fraction of photosynthetically active radiation (fAPAR) absorbed by plant canopy [28,29]. The rice plant variables GPP, LAI, NDVI, and CCC were used as rice growth indicators in this study. The GPP can be simulated using a light use efficiency model [30] with the photosynthetically active radiation (PAR) absorbed by canopy chlorophyll [31]. Based on these relations and assuming other factors constant across biochar treatments, we inferred the relative GPP variation ($\Delta GPP/GPP$) after biochar application from the variation in NDVI and CCC using a propagation approach [32, see Supplementary material for further details]:

$$\frac{\Delta GPP}{GPP} = \frac{\Delta NDVI}{NDVI} + \frac{\Delta CCC}{CCC}. \tag{3}$$

2.4.4 Estimation of shortwave surface albedo and directional emissivity

The shortwave surface albedo was estimated from the PRO4SAIL model results following the method in [33]:

$$\alpha = \frac{\alpha_{model}}{\bar{R}_{model}}\bar{\mathrm{R}}, \tag{4}$$

where $\bar{\mathrm{R}}$ and $\bar{R}_{model}$ are the Cubert-measured and PRO4SAIL-modelled mean blue-sky directional reflectance from wavelength 450 nm to 950 nm respectively; α_{model} is PRO4SAIL-modelled shortwave surface albedo.

The directional land surface emissivity was calculated from the canopy gap fraction following François [34]:

$$\varepsilon_s(\theta_V) = 1 - b(\theta_V)(1-\sigma_f)(1-\varepsilon_g) - c[1-b(\theta_V)(1-\sigma_f)](1-\varepsilon_v), \tag{5}$$

where θ_V is the thermal camera viewing direction, with $\theta_V = 0$ for nadir-viewing; ε_v and ε_g are leaf emissivity and bare ground emissivity respectively, and in this work $\varepsilon_v = 0.98$ and $\varepsilon_g = 0.94$ were used; c is a cavity factor, accounting for the volumetric multiple scattering inside rice canopy, and c = 0.3 was used for nadir viewing; b(θ_V) is the directional gap fraction at viewing direction θ_V; σ_f is called shading factor and $1-\sigma_f$ is the hemispherical transmittance. Both b(θ_V) and σ_f were estimated from LAI. See Supplementary material for further details. The estimation of hemispherical-directional emissivity in Eq. (7) has been shown to have high computation efficiency and high accuracy [34].

2.4.5 Estimation of land surface temperature

The land surface temperature (T_s) was estimated from the brightness temperature with a correction for the reflected longwave radiation by land surface:

$$T_s = \left[\frac{{T_b}^4-(1-\varepsilon_s)\varepsilon_a {T_a}^4}{\varepsilon_s}\right]^{1/4}, \tag{6}$$

where T_a is the air temperature from the weather station, [K]; ε_s is the land surface emissivity estimated from Eq. (5) for $\theta_V = 0$; ε_a is the atmosphere emissivity, estimated from air temperature and relative humidity following Prata [35]. For details see [36].

2.4.6 Energy components and variations in WUE

Net radiation R_n [W/m²], the difference between incident and outgoing radiation energy, was calculated as:

$$R_n = (1-\alpha)R_s + \sigma\varepsilon_s\varepsilon_a T_a^4 - \sigma\varepsilon_s T_s^4, \tag{7}$$

where R_s is the incoming solar radiation measured by the weather station at the site, W/m²; α is the land surface albedo derived from Eq. (4); $\sigma = 5.67\times10^{-8}$ W/m²/K⁴, Stefan–Boltzmann constant. T_s, T_a, ε_s, and ε_a have the same definitions as in Eq. (6).

Latent heat flux (λET, [W/m²], the ET in energy form) was estimated as the residual component of the surface energy balance:

$$\lambda ET = R_n - H - G, \tag{8}$$

where R_n is the net radiation from Eq. (7), H [W/m²] is sensible heat flux, and G [W/m²] is the heat storage flux in soil and plants. G is estimated from net radiation R_n and fractional vegetation cover f_c using an empirical equation in [37]:

$$G = R_n[0.315(1-f_c) + 0.05f_c], \tag{9}$$

where f_c is calculated from the aforementioned directional gap fraction at nadir-viewing direction (see Supplementary material): $f_c = 1 - b(0) = 1 - e^{-0.245LAI}$.

The sensible heat flux H was estimated from the temperature difference between the land surface and the air using the bulk transfer equation:

$$H = \rho C_p \frac{T_s - T_a}{r_a + r_{ex}}, \tag{10}$$

where ρ is the air density; C_p is the specific heat of air at constant pressure; and r_a is aerodynamic resistance to heat transfer, estimated from wind speed and the average height of rice canopy following [38]; r_{ex} is an extra resistance added to r_a for correcting the difference between radiometric temperature and aerodynamic temperature in sensible heat flux calculation. r_{ex} is approximated by $5.75/u_*$ [39,40], where u_* is friction velocity. Note that Eq. (10) uses the surface temperature as a proxy of aerodynamic temperature, even though r_{ex} is introduce to account for this, underestimates on r_{ex} may result in an overestimation of the sensible heat flux for bare soil area from an overestimated aerodynamic temperature, and subsequently results in negative evapotranspiration in Eq. (10). When this happened, we assigned a zero value for evapotranspiration (reasonable for dry bare soil) and recalculated sensible heat flux H using Eq. (8). The available energy (AE, [W/m²]) was estimated as the difference between net radiation R_n and the ground heat flux G, i.e. $AE = R_n - G$. Evaporative fraction (EF, [-]) is the latent heat flux normalized by the available energy: $EF = \lambda ET/AE$.

The variations in WUE after biochar application were inferred from differences between the GPP variation and the ET variation using variation propagation method again (see Supplementary material for further details):

$$\frac{\Delta WUE}{WUE} = \frac{\Delta GPP}{GPP} - \frac{\Delta ET}{ET}. \tag{11}$$

2.4.7 Soil moisture content and soil matric potential estimation

We estimated soil moisture content from UAV data using a temperature-vegetation dryness index [TVDI, 41], a triangle method by identifying the pixel dryness from the space of temperature variations between surface and bulk atmosphere ($\Delta T = T_s - T_a$) and fractional vegetation cover f_c, and then related TVDI to soil moisture content in the root zone as shown in [36]:

$$TVDI = \frac{\Delta T - \Delta T_{min}}{\Delta T_{max} - \Delta T_{min}} = 1 - \frac{\theta - \theta_{WP}}{\theta_{FC} - \theta_{WP}}, \tag{12}$$

where ΔT_{max} and ΔT_{min} are the dry and wet edges of the ΔT-f_c triangle, estimated following [42]; and θ [% in m^3/m^3] is the soil moisture content to be estimated. θ_{FC} and θ_{WP} are soil moisture content at field capacity and wilting point respectively, estimated from soil water retention curve at soil matric potential of -0.05 and -1.5 MPa respectively (see [25] for details of water retention curve estimation using in situ measurements). The spatially explicit soil matric potential (ψ, [MPa]) was then estimated from the UAV-derived soil moisture content using the Van Genuchten model [43]:

$$\psi = \frac{1}{\alpha_v}\left(\frac{1}{\Theta^{1/m}} - 1\right)^{1/n}, \tag{13}$$

where $\Theta = \frac{\theta - \theta_r}{\theta_s - \theta_r}$, $m = 1 - \frac{1}{n}$, and θ_r, θ_s, α_v, and n are the water retention curve parameters reported in [25].

2.4.8 Statistical analysis

The biophysical and land surface variables derived from UAV hyperspectral and thermal sensing were summarized for each plot to assess their relative changes after biochar application. The sunlit soil, shaded soil, and rice canopy pixels were identified using unsupervised classification [44]. The sunlit and shaded leaves were not separable and the whole canopy was considered as a turbid medium in PRO4SAIL model [45]. Sunlit soil pixels at plot corridors were extracted for analyzing the biochar effects on bare soil albedo and surface temperature. Rice canopy pixels were extracted for analyzing the biochar effects on root zone soil moisture, canopy biophysical variables, and canopy surface energy components. To reduce edge effects [46], the pixels within 15 cm to borders of each plot, roughly corresponding to the edge rows of rice plants, were discarded. The valid pixels extracted from each plot were aggregated to three sub-plots (Figure 1) for further statistical analysis, to avoid spatial autocorrelation from fine resolution.

We analyzed four days' repeated UAV results over three treatment groups with triplicate using repeated measures [47] analysis of variance (ANOVA) by the free statistic software JASP (available at https://jasp-stats.org/). The greenhouse-Geisser correction was used if sphericity had been violated in the repeated measures. The marginal mean and standard error of each variable were calculated for each group of three plots and four days considering the degrees of freedom within- and between-subjects. The mean variable differences between the treatment groups and the control group were analyzed using Tukey's honest significant difference test [48]. For the one-time measurement of leaf and soil samples, one-way ANOVA was used to analyze if their mean values were different. The four days' repeated UAV results were compared with the *in situ* measured soil water content and soil matric potential using violin plots and descriptive plots with mean and 95% confidence interval. A simple Pearson correlation was used to test the relationships between key rice growth variables and soil water availability.

3. Results

Preprints (www.preprints.org) | NOT PEER-REVIEWED | Posted: 9 April 2021 doi:10.20944/preprints202104.0267.v1

3.1. Hyperspectral and thermal imagery

We obtained orthomosaic Cubert hyperspectral images of 4.5 mm resolution in this field campaign. Figure 2a shows an example of a false-color composite image taken on November 14, 2018. Individual rice leaf blades are visible. Figure 2b shows the comparison of hyperspectral reflectance curves measured by Cubert camera (after the empirical line correction) and ASD spectroradiometer on rice canopy. The two curves share a similar spectra pattern and show the reliability of UAV-based hyperspectral sensing in the campaign. Note that the last few bands of Cubert camera have large variations and were discarded from further analysis following the manufacturer's recommendation. In four days' measurements, the assumed static dark soil and white metal box objects had up to 30 % deviations from day to day (Figure 2 c and d), indicating the necessity for correcting the systematic day-to-day reflectance drift to obtain comparable results from the hyperspectral camera. The PRO4SAIL model using normalized hyperspectral reflectance resulted in an average high R^2 of 0.96 and a low root-mean-squared-difference of 0.02 between the UAV-measured and the Pro4SAIL-modeled hyperspectral reflectance (Figure S1).

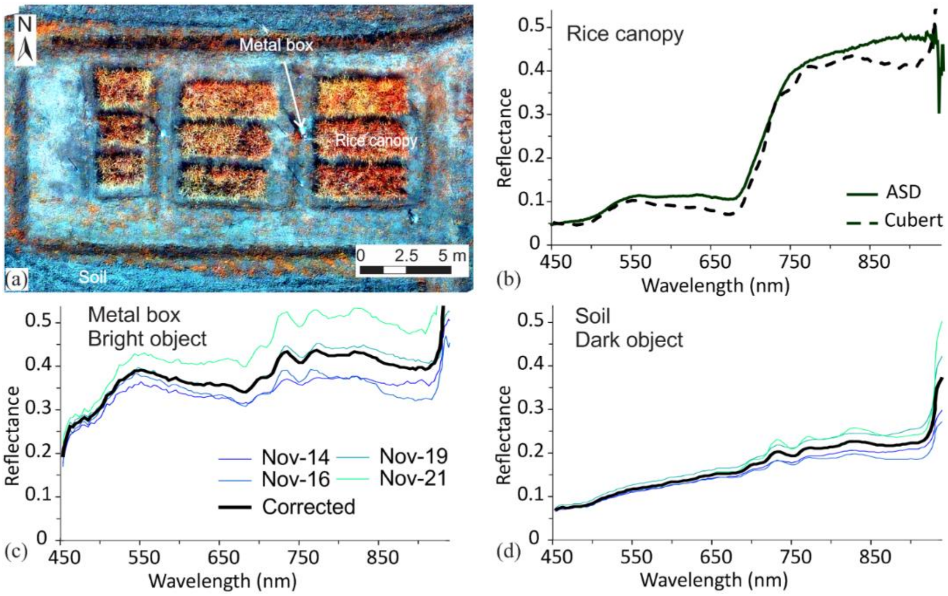

Figure 2. (a) False-color composite image from Cubert hyperspectral camera band 104, 29, and 12. Red color denotes vegetation and blue color bare soil. (b) Comparison of rice canopy reflectance measured by ASD spectroradiometer and Cubert camera after the empirical line correction using (c) reflectance of dark soil object, and (d) reflectance of bright metal box object (black line) in four days measurement (colored lines).

The land surface radiometric temperature (LST) map (Figure 3) shows warmer bare soil and cooler green rice canopy during the local noontime flight on November 16, 2018, matching well with the land covers in Figure 2 false-color image. The air temperature was 26.7 °C at the flight time and 99 % of the LST in the area was within 29.1 to 42.4 °C. The LST histogram of whole area was bimodal, with two peak temperatures at 31.6 and 36.5 °C, corresponding to vegetation and bare soil respectively. The LST histogram of rice plots showed only one peak at 30.9 °C. Since all the parameters in the PRO4SAIL model were set for the rice canopy, the output LAI and subsequently estimations of albedo and emissivity may not fit other vegetation types in the research area. Therefore, to avoid possible large errors, we only analyzed and presented the results of rice plots in the following sections.

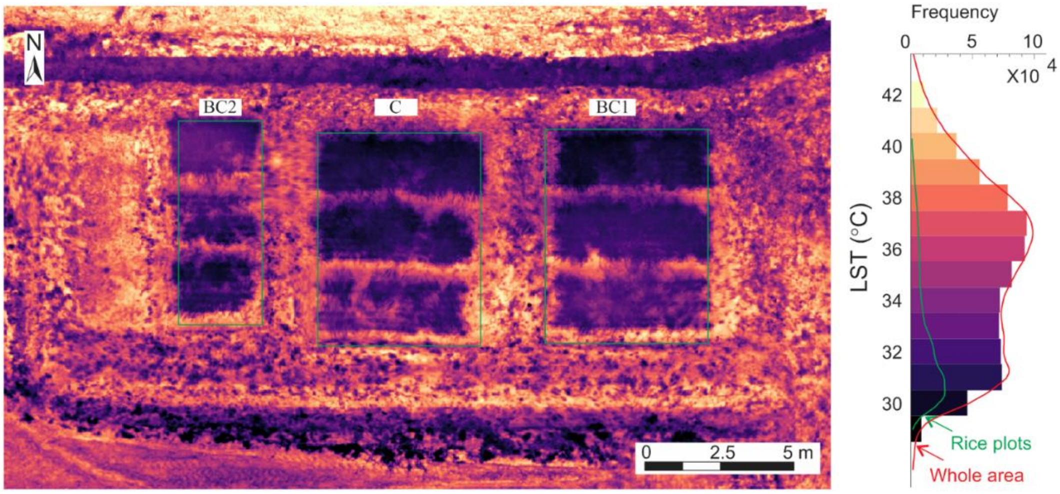

Figure 3. Land surface temperature (LST, 2.25 cm resolution) at 12:30 on November 16, 2018 estimated from the FLIR tau2 thermal camera and the Cubert-derived land surface emissivity. The yellow color indicates hot pixels and the dark color cool pixels.

Combining the temperature and hyperspectral reflectance from UAV, and the auxiliary data from ground measurements, including weather station data, leaf water content, concentrations of leaf nutrients and soil total nitrogen, and soil water retention curve, we mapped soil moisture content, soil matric potential, leaf and canopy properties, and energy components over the three experimental groups. The average changes of key variables after biochar application are summarized in Table 1. Detailed information is given in Table S1 of Supplementary Material.

3.2. Variations in soil variables after biochar application

Figure 4a shows the map of soil moisture content in the three groups BC1, BC2, and C. The UAV-derived average soil moisture content was significantly higher in biochar amended soils BC1 by 17.7±0.1 % and BC2 by 10.8±0.1 % compared with the control (Table 1). The soil moisture content measured by *in situ* sensors showed overall higher values in biochar groups than in the control, but the spatial variations within group were large (Figure 4b, c, Figure S2) and those changes were not statistically significant (Table S1). UAV-derived soil matric potential was significantly higher in BC1 biochar by 44.8±0.7 % and lower in BC2 biochar by −66.9 ±0.7 % than the control (Table 1, Figure 5, Figure S3). The soil matric potential measured by *in situ* sensors did not vary across treatments (Table S1) and the range of spatial variation was also large, from -1.4 to -0.2 MPa (Figure S3), contrasting to the UAV-derived soil matric potential of about -0.45 to -0.06 MPa. The fitted soil water retention curves of biochar groups shifted towards higher soil water content at a given water potential compared to the control (Figure S4a).

The average soil surface albedo values were significantly higher in the two biochar groups, and the soil surface temperature decreased by −0.7±0.2 % in BC1 and −1.4±0.2 % in BC2. Measurements on soil samples revealed non-significant changes in soil total nitrogen concentration (Table S1).

Table 1. Average changes (%) in key variables of biochar groups compared with the control (marginal mean±SE) derived from UAS derived data. Bold fonts indicate the variations significant at $p < 0.05$.

Variables		Bamboo biochar BC1 (%)	Sugarcane biochar BC2 (%)
Soil variables	Soil moisture content from UAS	**17.7±0.1**	**10.8±0.1**
	Soil matric potential from UAS[1]	**44.8±0.7**	**−66.9 ±0.7**

	Soil albedo	**0.5±0.1**	**1.4±0.1**
	Soil surface temperature	**−0.7±0.2**	**−1.4±0.2**
Leaf and canopy variables	Gross primary production	**41.9±3.4**	**17.5±3.4**
	Normalized difference vegetation index	**10.0±1.4**	**7.4±1.4**
	Canopy chlorophyll content	**32.0±3.0**	**10.1±3.0**
	Water use efficiency	**40.8±3.5**	**13.4±3.5**
	Leaf area index	**6.0±1.3**	**−4.9±1.3**
Land surface energy components	Net radiation	−0.2±0.3	**2.3±0.3**
	Latent heat flux (evapotranspiration)	1.1±1.0	**4.0±1.0**
	Evaporative fraction	**3.7±1.0**	− 0.2±1.0
	Ground heat flux	**−1.8±0.6**	**3.5±0.6**
	Sensible heat flux	−0.4±0.7	−0.4±0.7

[1] From the UAS-derived soil moisture content and the *in situ* sensor-derived soil water retention curve.

3.3. Variations in rice leaf and canopy variables after biochar application

There were significant increases in canopy GPP, NDVI, chlorophyll content, and WUE in the biochar groups compared to the control (Table 1 and S1; Figure 6). Opposite changes were observed in LAI, fractional vegetation cover (f_c), and canopy LST in two biochar groups. The LAI and f_c were significantly higher in BC1 but lower in BC2. The canopy LST significantly decreased by −0.6±0.2 % in BC1 and increased by 0.6±0.2 % in BC2, along with a significant decrease in canopy albedo only in BC2 (−3.1±0.5 %). Leaf sample analyses on November 19, 2018 revealed non-significant changes in leaf water and leaf P concentration, whereas the leaf K concentration was significantly higher in both biochar groups, and the leaf N concentration was significantly higher only in the BC1 group (Table S1) compared with the control.

3.4. Variations in evapotranspiration and land surface energy components

The net radiation, latent heat flux (or evapotranspiration), and ground flux were significantly higher in BC2 by 2.3±0.3 %, 4.0±1.0 %, and 3.5±0.6 % respectively than in the control. The ground heat flux significantly decreased by −1.8±0.6 % in BC1, and the evaporative fraction was 3.7±1.0 % higher in this group than in the control. There were no significant differences in sensible heat flux among treatments (Table 1, Figure 7).

Preprints (www.preprints.org) | NOT PEER-REVIEWED | Posted: 9 April 2021 doi:10.20944/preprints202104.0267.v1

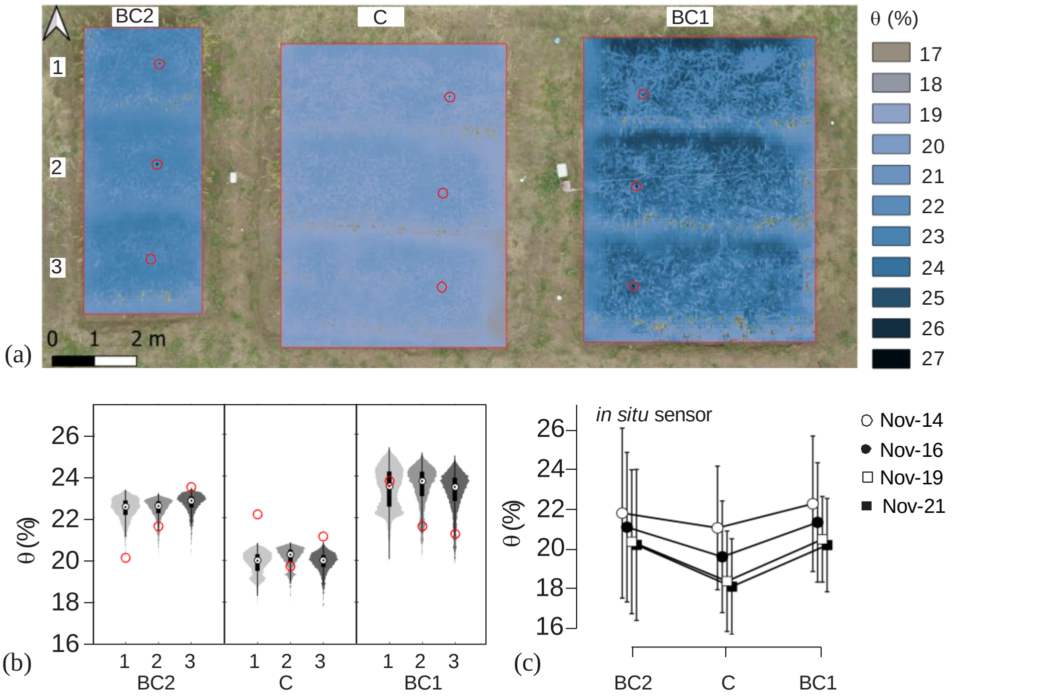

Figure 4. (a) Map of soil moisture content (θ) of three experimental groups from UAS on November 14, 2018. The circle (○) denote sensor locations. (b) Violin plots of the θ from UAS in each plot and each treatment. The shaded areas of the violin plot denote the distribution of the day's measurement, the white dots denote the median values, and the bottom and top edges of the black bars denote the 25th and 75th percentiles respectively. The circles (○) denote sensor measurements during flight (c) The comparison of plot-averaged θ in three groups BC1, BC2, and C from in situ sensors during the four-day campaign. Whiskers denote 95 % confidence interval of each group on each day.

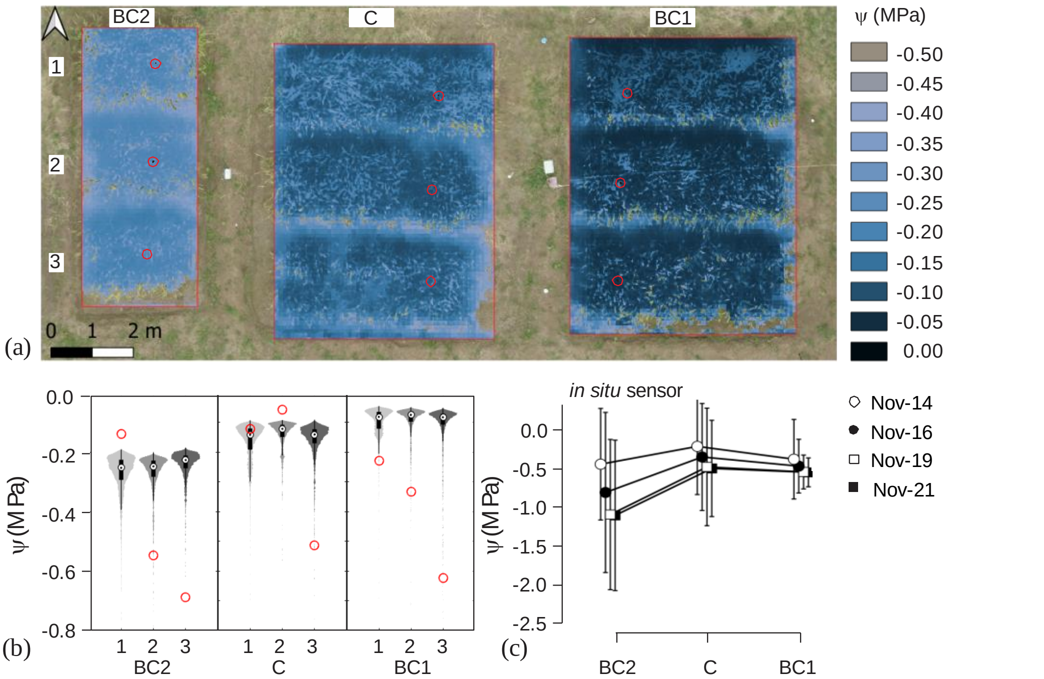

Figure 5. (a) Map of soil matric potential (ψ) of three experimental groups from UAS on November 14, 2018. The circle (○) denote sensor locations. (b) Violin plots of the ψ from UAS in each plot and each treatment. The shaded areas of the violin plot denote distribution of the day's measurement, the white dots denote the median values, and the bottom and top edges of the black bars denote the 25th and 75th percentiles respectively. The circles (○) denote sensor measurements dur-

Preprints (www.preprints.org) | NOT PEER-REVIEWED | Posted: 9 April 2021 doi:10.20944/preprints202104.0267.v1

ing flight (c) The comparison of plot-averaged ψ in three groups BC1, BC2, and C from in situ sensors during the four-day campaign. Whiskers denote 95 % confidence interval of each group on each day.

3.5. Comparison of key rice biophysical variables with soil matric potential

Over the experimental plots, the canopy chlorophyll content, NDVI, and LAI were correlated with the soil matric potential with R^2 of 0.16, 0.12, and 0.32 respectively (Figure 8). The canopy chlorophyll content, NDVI, and LAI had correlations with soil moisture content with relatively lower R^2 of 0.12, 0.09, and 0.12 respectively (Figure S5).

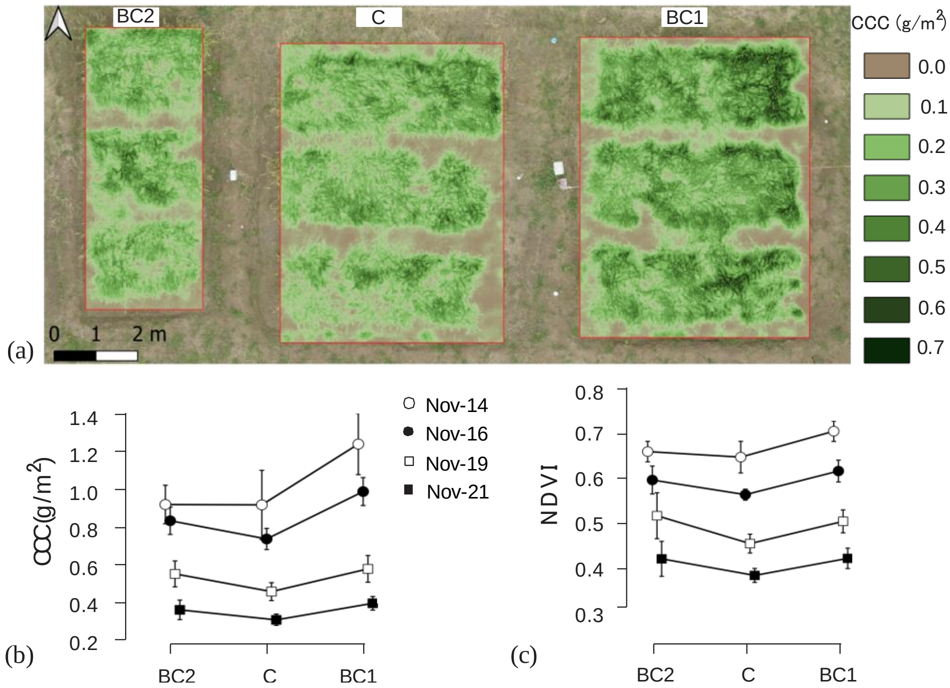

Figure 6. (a) Map of canopy chlorophyll content (CCC) over three experimental groups. The comparison of three groups BC1, BC2, and C is shown in (a) CCC from Cubert, and (b) normalized difference vegetation index (NDVI). Whiskers denote 95 % confidence interval of each group on each day.

3.6. Comparison of evaporative fraction with soil moisture content and matric potential

The evaporative fraction (EF=latent heat flux/available energy) had strong correlations with soil moisture content (θ) in individual groups (R^2 = 0.87, 0.78, and 0.82 for group C, BC1, and BC2 respectively, Figure 9). The ET-θ fitting lines of two biochar groups BC1 and BC2 shifted toward higher θ compared with the control group C. The slopes of the fitting lines were 0.29, 0.15, and 0.30 for group C, BC1, and BC2 respectively. The evaporative fraction had strong exponential relationships with soil matric potential (ψ) in individual groups (Figure S4b), with the EF-ψ fitting line shifting toward higher ψ after BC1 biochar application and toward lower ψ after BC2 biochar application.

Preprints (www.preprints.org) | NOT PEER-REVIEWED | Posted: 9 April 2021 doi:10.20944/preprints202104.0267.v1

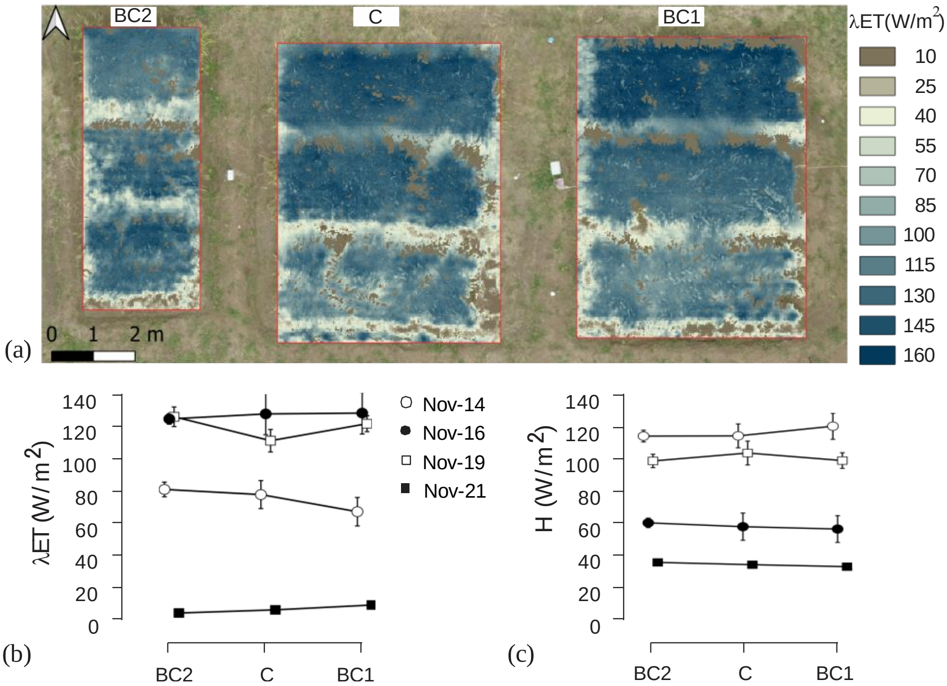

Figure 7. (a) Map of latent heat flux (λET) over three experimental groups. The comparison of three groups BC1, BC2, and C is shown in (b) latent heat flux (λET), and (c) sensible heat flux (H). Whiskers denote 95% confidence interval of each group on each day.

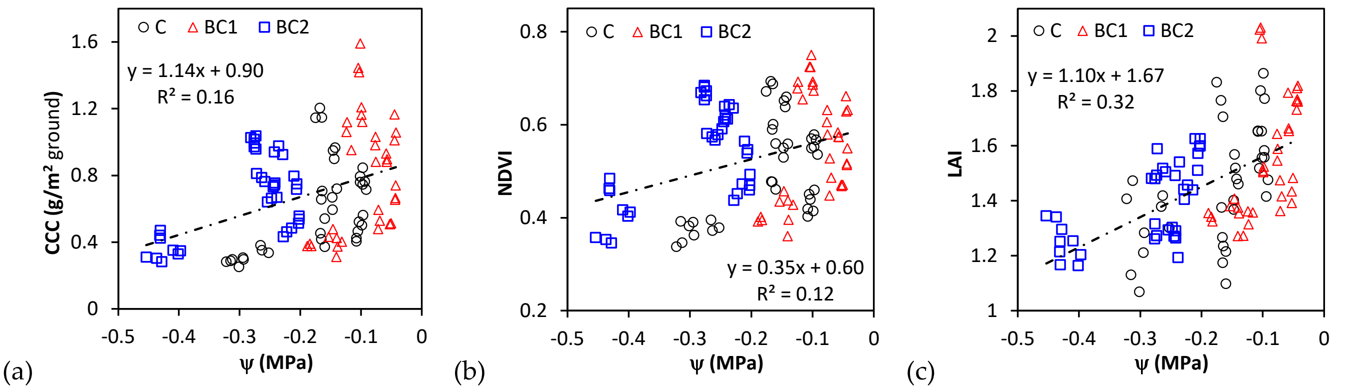

Figure 8. Overall relationships between soil matric potential (ψ) and (a) canopy chlorophyll content (CCC), (b) normalized difference vegetation index (NDVI), and (c) leaf area index (LAI) in the three groups BC1, BC2, and C.

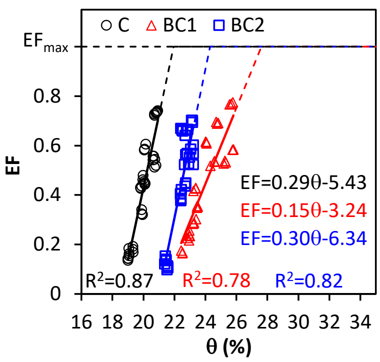

Figure 9. Relationships between evaporative fraction (EF) and soil moisture content (θ) derived from UAS for three groups BC1, BC2, and C. Dash lines indicate the extrapolation of the fitting lines to maximum EF (EF_{max}≤1).

4. Discussion

This study combined UAV-based hyperspectral and thermal imagery with ground measurements and physical models to provide a comprehensive assessment of relative changes in upland rice growth, soil water availability, and WUE after biochar application. We found that in two biochar groups, rice GPP, NDVI, chlorophyll content, soil moisture content, and WUE were significantly higher than the control group. The increments were larger in the bamboo biochar group (BC1) that also had higher leaf nitrogen concentration. We found opposite behaviors between BC1 and BC2 during the period for soil matric potential, leaf area index, and fractional vegetation cover, which increased in the bamboo biochar group (BC1) but decreased in the sugarcane biochar group (BC2, Table 1). Looking at surface energy fluxes, the net radiation, latent heat flux (evapotranspiration), and ground heat flux significantly increased in sugarcane biochar groups (BC2), but not in the bamboo biochar group (BC1), which translated in a significant increase in the evaporative fraction in BC1, but no change in BC2 compared to the control plots. From the exposed soil surfaces between plots, we did not observe lower soil surface albedo after the biochar application at a rate of 0.4 % (weight/weight) within 20 cm topsoil in our experiment. The biochar had been added to the soil for eleven months in BC1 and five months in BC2, so the charcoal particles were likely already incorporated into the soil by the time the measurement campaign was conducted, thereby limiting any direct soil albedo effect from biochar. Our albedo results contrast sharply with other studies that used large-scale dark soil simulations or laboratory experiments and claimed that biochar addition could decrease soil surface albedo and increase radiative forcing feedback to climate [e.g. 49,50].

4.1. Biochar effects on soil water availability

Biochar addition has been shown to alter soil moisture content, and soil physical and hydraulic properties [16,17]. We found from in situ sensor measurements, one point in each plot, that the soil moisture content (θ) was higher in both biochar plots but differences across treatments were not significant due to the large within-group variability. Using the UAV-derived θ that covered the whole area of each plot to better account for the variability within each plot, we found significant increases in θ in biochar-amended plots (Figure 4). This demonstrated the advantage of high-resolution drone-based remote sensing approach over ground point measurements in cropland and agricultural assessment.

The significantly higher θ in biochar groups than the control was probably due to the increase in water holding capacity in biochar amended soil. The higher water holding capacity is likely linked to the porous biochar structure that increases the particle surface area, so that more water can be retained by the soil. The increased water retention with biochar addition can also reduce nutrient leaching [51], and result in more efficient plant nutrient uptake [20]. This might partly explain the higher leaf nitrogen concentration observed in the bamboo biochar group (BC1).

It should be noted that the θ derived from temperature-vegetation relationships reflects the water availability in the whole root zone [36], and the rice rooting depth can reach 0.5-1.0 m [38], far deeper than the depth of 15 cm at which the *in situ* sensors were placed in this study. The shallower the measurement location, the stronger the influence from atmospheric forcing and consequently the larger the fluctuations of the measurements, explaining the higher variability of the *in situ* measurements compared to the remote sensing estimates. Besides, the groundwater level was reported 0.8 m below the surface during the dry period [25] and the capillary rise in clay loam soil of the site might dampen the fluctuations of root zone soil moisture. The mismatch of *in situ* sensor-measured and UAV-derived θ makes the two sets of data not readily comparable.

The soil matric potential presented a different picture for the two biochar applications, increasing in the bamboo biochar application (BC1) and decreasing in the sugarcane biochar application (BC2), contrary to the θ that increased in both biochar applications. Along with the decreased soil matric potential in BC2, the BC2 plots had lower leaf nitrogen concentration, LAI, GPP, and WUE. Apart from the biochar feedstock difference between BC1 and BC2, [25] attributed the lower plant performance to the shorter time of sugarcane biochar settlement in soil. The bamboo biochar had been applied six months earlier and might have a better establishment in soils.

4.2. Biochar effects on rice growth indicators

We found that rice GPP, NDVI, and CCC were higher in both biochar applications than in the control group (Figure 6). A similar positive effect of biochar addition on maize was reported by Agegnehu, *et al.* [52] under Australian tropical dry conditions. We indirectly inferred the changes in plant production from the changes in NDVI, a proxy of the fraction of photosynthetic energy absorbed by the canopy [28,29], and the changes in canopy chlorophyll content that determines the plant photosynthetic capacity and therefore maximum potential light use efficiency. Ultimately, all these positive changes in canopy properties might be traced back to the aforementioned improvement in soil water availability and subsequently the resilience of plant to dry spells after biochar application in the arid cropland, which was also supported by the results of isotopic composition of plant water [25].

A further correlation analysis showed that soil matric potential was a slightly better predictor of variations in CCC, NDVI, and LAI than the θ (Figure 8 and S5). Vascular plants absorb soil water and transport it through the xylem to the leaf surface thanks to the gradients of water potential along the soil-plant-atmosphere continuum [SPAC, 53,54]. Assuming a steady-state flow along the SPAC, higher water availability as indicated by higher soil water potential will result in more water transported to the leaves, which guarantees higher leaf water potential and gas exchanges [53]. In turn, this improved water status is expected to allow for larger leaf area and photosynthetic capacity, thereby explaining the observed correlations.

4.3. Biochar effects on evaporative fraction and plant WUE

We found that the rate of change of the evaporative fraction (EF; i.e., the fraction of energy converted to latent heat) with soil moisture content in the bamboo biochar (BC1) group was about half of that in the other groups, indicating that the rice in BC1 group was less sensitive to soil moisture changes at a relatively higher moisture level. If the EF-θ fitting curve can be extrapolated to the line of EF = EF_{max}, the intersection points will be at higher soil moisture contents in the two biochar amendment groups (Figure 9). This suggests that rice growing in biochar amended soil reduced the evaporative fraction at any given soil saturation below the point of incipient stomatal closure compared to the control, in agreement with the model results in [17, Fig. 4B]. This pattern can also be interpreted in a different way—that biochar-amended soils hold more water, but trigger stomatal closure and reduced evapotranspiration at relatively higher soil moisture compared to control plots. In other words, despite holding more water, biochar-amended soils exhibited water availability comparable to control plots. Indeed, water potential varied in inconsistent ways with biochar amendment (Figure 5).

We found that EF increased nonlinearly with soil matric potential (ψ) in each group (Figure S4b) and may be fitted using sigmoidal curves [55]. The EF-ψ fitting curve of sugarcane biochar (BC2) group shifted toward lower ψ compared to the control, suggesting a higher evaporative fraction at a given ψ in BC2. Indeed, BC2 had the highest evapotranspiration among all three experimental groups (Table S1).

However, the average EF in BC2 was slightly lower than the other two groups during the UAV campaign period, indicating that the rice in this group was relatively water-stressed. Correspondingly, the rice canopy surface temperature, an indicator for instantaneous plant water stress [56], was slightly higher in BC2 than the other two groups (Table S1). Moreover, the leaf water content, an indicator for sustained water stress [10], was the lowest in BC2 among the three groups. Although these differences between the biochar groups and the control were generally small in magnitude during the campaign days, if the mild plant stress had been accumulated over time, it could lead to significantly inferior rice growth, explaining the lower LAI and canopy cover in BC2 compared with the control.

How could the biochar amendment affect plant WUE? The answer to the question is very critical to crops in water-limited areas where the experiment locates. In the review by Fischer et al. [17], few studies reported a positive effect of biochar on crop WUE based on yield. Plant WUE is expected to increase if the biochar promotes plant production without a significant increase in evapotranspiration. This is the case for the bamboo biochar group, where the gross primary production (GPP) increased significantly and the evapotranspiration did not change. If the GPP increases at a significant cost of evaporative water loss, the plant WUE will change depending on which (GPP or evapotranspiration) increases more. This is the case for the sugarcane biochar group, where the GPP increased along with the significant increase in evapotranspiration. The GPP increment largely surpassed the increment of evapotranspiration and the consequent WUE was increased as well in the sugarcane biochar group. This result is key as it provides observational evidence on the influence of biochar for WUE, suggesting the amendment would potentially benefit climate-smart agriculture by adding resilience to crops in regions with limited water resources [17,18].

5. Conclusions

This study demonstrated that the hyperspectral and thermal imagery from UAV is promising to provide a wide range of indicators for quantifying upland rice growth and water usage after biochar application. We showed that the indicators derived from the imagery using physical models were useful in exploring biophysical information behind indirect measurements, and in explaining the mechanisms from the observed changes after biochar application. The integration of direct and indirect measurements allows the identification of relative changes in plant biophysical variables, soil water availability, and surface energy fluxes. Drone-based remote sensing provided spatially explicit information without disturbing the measurement target, densifying ground point measurements from sensors or laboratory samples, enabling a wide range of applications that can benefit precision agriculture and crop management in general.

The results show relatively large increases in GPP, chlorophyll content, soil moisture content after the biochar amendments. In addition, non-significant or significant but small changes in energy fluxes and evapotranspiration were determined, suggesting increases in WUE after biochar application. However, the biochar feedstock and application management might have influenced the outcomes as in our case the increment in bamboo biochar amended soil was larger than in sugarcane biochar amended soil.

This study motivates a larger scale experiment so that other aspects related to the impact of the amendment for WUE, GPP, and soil fertility can be tested at a full crop scale. The results demonstrate the potential of biochar for agricultural water management to withstand dry spells by allowing rice plants to optimize water and nutrients use. A noteworthy result is that potential climate feedbacks derived from dark soil mimicking and laboratory tests might not be as significant as thought, based on the detected changes in the surface energy balance components affecting radiative forcing such as the land surface temperature, albedos, or sensible heat fluxes. Biochar amendment is promising as part of the strategies oriented to improve the resilience of crops under rainfall reduction scenarios associated with the impacts of climate variability and change. Furthermore, its capacity to induce negative carbon emissions adds value to the amendment. We highlight the promising role of biochar as a strategy for sustainable farming and climate change mitigation.

Supplementary Materials: The following are available online at www.mdpi.com/xxx/s1, Figure S1-S5, Table S1.

Author Contributions: Conceptualization, M.G., S.M., S.L., and M.J.; methodology, C.K., and B.F.; software, C.K. and H.J.; validation, M.G., S.M., and A.D.. formal analysis, H.J. and M.G.; investigation, C.K., B.F., J.R.,L.M., A.D., and A.S.; data curation, C.K..B.F. and J.R.; writing—original draft preparation, H.J.; writing—review and editing, M.G., B.F., S.M., A.D. and H.J.; visualization, H.J.; supervision, M.G., S.M., S.L., A.S. and M.J.; project administration, M.G., S.M., S.L., A.S. and M.J.; funding acquisition, M.G. All authors have read and agreed to the published version of the manuscript.

Funding: This research was funded by the Joint Call of the Water Joint Programming Initiative (Water JPI) and the Joint Programming Initiative on Agriculture, Food Security and Climate Change (FACCE-JPI) of the European Union and partner countries via the Agricultural Water Innovations in the Tropics (AgWIT) project. HJ is jointly funded by Sino-Danish Center for Education and Research (SDC), Denmark. SM acknowledges support from the Swedish Research Council (Vetenskapsrådet), Formas, and Sida (VR 2016-06313), and by the Bolin Centre for Climate Research (Research Area 7).

Acknowledgments: We thank all the people who helped in the field and the laboratory, especially Edwin Quirós Ramos, Roberto Ramírez, Juan Carlos Jiménez Vargas, Paolo Delgado Chavarría, and all technical staff from the EEEJN-INTA who helped develop the rice experimental design and advised about regional crop management practices. Also, we want to thank the students Sharon Arce, Johnny Arriola, and Katherine Sánchez of Universidad Nacional, Liberia, Costa Rica.

Conflicts of Interest: The authors declare no conflict of interest."

References

1. Oliveira, R.A.; Nasi, R.; Niemelainen, O.; Nyholm, L.; Alhonoja, K.; Kaivosoja, J.; Jauhiainen, L.; Viljanen, N.; Nezami, S.; Markelin, L.; et al. Machine learning estimators for the quantity and quality of grass swards used for silage production using drone-based imaging spectrometry and photogrammetry. *Remote Sens. Environ.* 2020, *246*, doi:10.1016/j.rse.2020.111830.
2. Dehkordi, R.H.; Denis, A.; Fouche, J.; Burgeon, V.; Cornelis, J.T.; Tychon, B.; Gomez, E.P.; Meersmans, J. Remotely-sensed assessment of the impact of century-old biochar on chicory crop growth using high-resolution UAV-based imagery. *Int. J. Appl. Earth Obs.* 2020, *91*, doi:10.1016/j.jag.2020.102147.
3. Radoglou-Grammatikis, P.; Sarigiannidis, P.; Lagkas, T.; Moscholios, I. A compilation of UAV applications for precision agriculture. *Computer Networks* 2020, *172*, 107148, doi:https://doi.org/10.1016/j.comnet.2020.107148.
4. Pipatsitee, P.; Eiumnoh, A.; Praseartkul, P.; Taota, K.; Kongpugdee, S.; Sakulleerungroj, K.; Cha-um, S. Application of infrared thermography to assess cassava physiology under water deficit condition. *Plant Production Science* 2018, *21*, 398-406, doi:10.1080/1343943x.2018.1530943.
5. Martynenko, A.; Shotton, K.; Astatkie, T.; Petrash, G.; Fowler, C.; Neily, W.; Critchley, A.T. Thermal imaging of soybean response to drought stress: the effect of Ascophyllum nodosum seaweed extract. *SpringerPlus* 2016, *5*, 1393, doi:10.1186/s40064-016-3019-2.
6. Berni, J.A.J.; Zarco-Tejada, P.J.; Sepulcre-Cantó, G.; Fereres, E.; Villalobos, F. Mapping canopy conductance and CWSI in olive orchards using high resolution thermal remote sensing imagery. *Remote Sensing of Environment* 2009, *113*, 2380-2388, doi:https://doi.org/10.1016/j.rse.2009.06.018.
7. Haboudane, D.; Miller, J.R.; Pattey, E.; Zarco-Tejada, P.J.; Strachan, I.B. Hyperspectral vegetation indices and novel algorithms for predicting green LAI of crop canopies: Modeling and validation in the context of precision agriculture. *Remote Sensing of Environment* 2004, *90*, 337-352, doi:https://doi.org/10.1016/j.rse.2003.12.013.
8. Tucker, C.J. Red and photographic infrared linear combinations for monitoring vegetation. *Remote Sensing of Environment* 1979, *8*, 127-150.
9. Zarco-Tejada, P.J.; Miller, J.R.; Morales, A.; Berjón, A.; Agüera, J. Hyperspectral indices and model simulation for chlorophyll estimation in open-canopy tree crops. *Remote Sensing of Environment* 2004, *90*, 463-476, doi:https://doi.org/10.1016/j.rse.2004.01.017.
10. Sobejano-Paz, V.; Mikkelsen, T.N.; Baum, A.; Mo, X.; Liu, S.; Köppl, C.J.; Johnson, M.S.; Gulyas, L.; García, M. Hyperspectral and Thermal Sensing of Stomatal Conductance, Transpiration, and Photosynthesis for Soybean and Maize under Drought. *Remote Sensing* 2020, *12*, 3182.
11. Yi, Q.; Huang, J.; Wang, F.; Wang, X. Evaluating the performance of PC-ANN for the estimation of rice nitrogen concentration from canopy hyperspectral reflectance. *International Journal of Remote Sensing* 2010, *31*, 931-940, doi:10.1080/01431160902912061.
12. Vitrack-Tamam, S.; Holtzman, L.; Dagan, R.; Levi, S.; Tadmor, Y.; Azizi, T.; Rabinovitz, O.; Naor, A.; Liran, O. Random Forest Algorithm Improves Detection of Physiological Activity Embedded within Reflectance Spectra Using Stomatal Conductance as a Test Case. *Remote Sensing* 2020, *12*, 2213.
13. Jacquemoud, S.; Verhoef, W.; Baret, F.; Bacour, C.; Zarco-Tejada, P.J.; Asner, G.P.; François, C.; Ustin, S.L. PROSPECT + SAIL models: A review of use for vegetation characterization. *Remote Sensing of Environment* 2009, *113*, S56-S66.
14. Mann, C.C. The Real Dirt on Rainforest Fertility. *Science* 2002, *297*, 920-923, doi:10.1126/science.297.5583.920.
15. Lehmann, J. Bio-energy in the black. *Frontiers in Ecology and the Environment* 2007, *5*, 381-387, doi:10.1890/1540-9295(2007)5[381:bitb]2.0.co;2.
16. DeLuca, T.H.; MacKenzie, M.D.; Gundale, M.J. Biochar effects on soil nutrient transformations. In *Biochar for Environmental Management: Science and Technology*, Lehmann, J., Joseph, S., Eds.; Earthscan, London, 2009; pp. 251-270.
17. Fischer, B.M.C.; Manzoni, S.; Morillas, L.; Garcia, M.; Johnson, M.S.; Lyon, S.W. Improving agricultural water use efficiency with biochar – A synthesis of biochar effects on water storage and fluxes across scales. *Science of the Total Environment* 2019, *657*, 853-862, doi:https://doi.org/10.1016/j.scitotenv.2018.11.312.
18. Lehmann, J. A handful of carbon. *Nature* 2007, *447*, 143-144, doi:10.1038/447143a.
19. Lehmann, J.; Rillig, M.C.; Thies, J.; Masiello, C.A.; Hockaday, W.C.; Crowley, D. Biochar effects on soil biota – A review. *Soil Biol. Biochem.* 2011, *43*, 1812-1836, doi:https://doi.org/10.1016/j.soilbio.2011.04.022.

20. Biederman, L.A.; Harpole, W.S. Biochar and its effects on plant productivity and nutrient cycling: a meta-analysis. *GCB Bioenergy* 2013, *5*, 202-214, doi:10.1111/gcbb.12037.
21. Jeffery, S.; Abalos, D.; Prodana, M.; Bastos, A.C.; van Groenigen, J.W.; Hungate, B.A.; Verheijen, F. Biochar boosts tropical but not temperate crop yields. *Environmental Research Letters* 2017, *12*, 053001, doi:10.1088/1748-9326/aa67bd.
22. Durán-Quesada, A.M.; Sorí, R.; Ordoñez, P.; Gimeno, L. Climate Perspectives in the Intra–Americas Seas. *Atmosphere* 2020, *11*, 959.
23. Maldonado, T.; Rutgersson, A.; Alfaro, E.; Amador, J.; Claremar, B. Interannual variability of the midsummer drought in Central America and the connection with sea surface temperatures. *Adv. Geosci.* 2016, *42*, 35-50, doi:10.5194/adgeo-42-35-2016.
24. Imbach, P.; Beardsley, M.; Bouroncle, C.; Medellin, C.; Läderach, P.; Hidalgo, H.; Alfaro, E.; Van Etten, J.; Allan, R.; Hemming, D.; et al. Climate change, ecosystems and smallholder agriculture in Central America: an introduction to the special issue. *Climatic Change* 2017, *141*, 1-12, doi:10.1007/s10584-017-1920-5.
25. Fischer, B.M.C.; Morillas, L.; Rojas Conejo, J.; Sánchez-Murillo, R.; Suárez Serrano, A.; Frentress, J.; Cheng, C.H.; Garcia, M.; Manzoni, S.; Johnson, M.S.; et al. Investigating the impacts of biochar on water fluxes in tropical agriculture using stable isotopes. *Hydrol. Earth Syst. Sci. Discuss.* 2020, *2020*, 1-47, doi:10.5194/hess-2020-404.
26. Deng, L.; Yan, Y.; Gong, H.; Duan, F.; Zhong, R. The effect of spatial resolution on radiometric and geometric performances of a UAV-mounted hyperspectral 2D imager. *ISPRS Journal of Photogrammetry and Remote Sensing* 2018, *144*, 298-314, doi:https://doi.org/10.1016/j.isprsjprs.2018.08.002.
27. Köppl, C.J. Thermal Imaging from Unmanned Airborne Vehicles. Technical University of Denmark (DTU), 2016.
28. Myneni, R.B.; Williams, D.L. On the relationship between FAPAR and NDVI. *Remote Sensing of Environment* 1994, *49*, 200-211, doi:http://dx.doi.org/10.1016/0034-4257(94)90016-7.
29. Sellers, P.J. Canopy reflectance, photosynthesis and transpiration. *International Journal of Remote Sensing* 1985, *6*, 1335-1372, doi:10.1080/01431168508948283.
30. Monteith, J.L. Solar radiation and productivity in tropical ecosystems. *The Journal of Applied Ecology* 1972, *9*, 747-766.
31. Zhang, F.; Zhou, G. Deriving a light use efficiency estimation algorithm using in situ hyperspectral and eddy covariance measurements for a maize canopy in Northeast China. *Ecology and Evolution* 2017, *7*, 4735-4744, doi:doi:10.1002/ece3.3051.
32. Jin, H.; Eklundh, L. In Situ Calibration of Light Sensors for Long-Term Monitoring of Vegetation. *Geoscience and Remote Sensing, IEEE Transactions on* 2015, *53*, 3405-3416, doi:10.1109/tgrs.2014.2375381.
33. François, C.; Ottlé, C.; Olioso, A.; Prévot, L.; Bruguier, N.; Ducros, Y. Conversion of 400-1100 nm vegetation albedo measurements into total shortwave broadband albedo using a canopy radiative transfer model. *Agronomie* 2002, *22*, 611-618, doi:DOI: 10.1051/agro:2002033.
34. François, C. The potential of directional radiometric temperatures for monitoring soil and leaf temperature and soil moisture status. *Remote Sensing of Environment* 2002, *80*, 122-133, doi:https://doi.org/10.1016/S0034-4257(01)00293-0.
35. Prata, A.J. A new long-wave formula for estimating downward clear-sky radiation at the surface. *Quarterly Journal of the Royal Meteorological Society* 1996, *122*, 1127-1151, doi:10.1002/qj.49712253306.
36. Wang, S.; Garcia, M.; Ibrom, A.; Jakobsen, J.; Josef Köppl, C.; Mallick, K.; Looms, M.C.; Bauer-Gottwein, P. Mapping Root-Zone Soil Moisture Using a Temperature–Vegetation Triangle Approach with an Unmanned Aerial System: Incorporating Surface Roughness from Structure from Motion. *Remote Sensing* 2018, *10*, 1978.
37. Su, Z. The Surface Energy Balance System (SEBS) for estimation of turbulent heat fluxes. *Hydrol. Earth Syst. Sci.* 2002, *6*, 85-100, doi:10.5194/hess-6-85-2002.
38. Allen, R.G.; Pereira, L.S.; Raes, D.; Smith, M. *Crop evapotranspiration: guidelines for computing crop water requirements, FAO Irrigation and Drainage Paper No. 56*; FAO, Rome, Italy, 1998; p. 300.
39. Norman, J.M.; Kustas, W.P.; Humes, K.S. Source approach for estimating soil and vegetation energy fluxes in observations of directional radiometric surface temperature. *Agricultural and Forest Meteorology* 1995, *77*, 263-293, doi:http://dx.doi.org/10.1016/0168-1923(95)02265-Y.
40. Boegh, E.; Soegaard, H.; Thomsen, A. Evaluating evapotranspiration rates and surface conditions using Landsat TM to estimate atmospheric resistance and surface resistance. *Remote Sens. Environ.* 2002, *79*, 329-343, doi:https://doi.org/10.1016/S0034-4257(01)00283-8.
41. Sandholt, I.; Rasmussen, K.; Andersen, J. A simple interpretation of the surface temperature/vegetation index space for assessment of surface moisture status. *Remote Sensing of Environment* 2002, *79*, 213-224, doi:https://doi.org/10.1016/S0034-4257(01)00274-7.
42. Garcia, M.; Fernández, N.; Villagarcía, L.; Domingo, F.; Puigdefábregas, J.; Sandholt, I. Accuracy of the Temperature–Vegetation Dryness Index using MODIS under water-limited vs. energy-limited evapotranspiration conditions. *Remote Sensing of Environment* 2014, *149*, 100-117, doi:https://doi.org/10.1016/j.rse.2014.04.002.
43. van Genuchten, M.T. A Closed-form Equation for Predicting the Hydraulic Conductivity of Unsaturated Soils. *Soil Science Society of America Journal* 1980, *44*, 892-898, doi:10.2136/sssaj1980.03615995004400050002x.
44. Guillén-Climent, M.L.; Zarco-Tejada, P.J.; Villalobos, F.J. Estimating Radiation Interception in Heterogeneous Orchards Using High Spatial Resolution Airborne Imagery. *IEEE Geoscience and Remote Sensing Letters* 2014, *11*, 579-583, doi:10.1109/lgrs.2013.2284660.
45. Verhoef, W. Light scattering by leaf layers with application to canopy reflectance modeling: The SAIL model. *Remote Sensing of Environment* 1984, *16*, 125-141.
46. Austin, R.B.; Blackwell, R.D. Edge and neighbour effects in cereal yield trials. *The Journal of Agricultural Science* 1980, *94*, 731-734, doi:10.1017/s0021859600028720.
47. Milliken, G.A.; Johnson, D.E. *Analysis of Messy Data. Volume 1: Designed Experiments*, 2nd edition ed.; Chapman & Hall/CRC: New York, NY, 2009.
48. Tukey, J.W. *Exploratory data analysis*; Addison Wesley Publishing Company Reading, Mass.: 1977.
49. Verheijen, F.G.A.; Jeffery, S.; van der Velde, M.; Penížek, V.; Beland, M.; Bastos, A.C.; Keizer, J.J. Reductions in soil surface albedo as a function of biochar application rate: implications for global radiative forcing. *Environmental Research Letters* 2013, *8*, 044008, doi:10.1088/1748-9326/8/4/044008.
50. Bozzi, E.; Genesio, L.; Toscano, P.; Pieri, M.; Miglietta, F. Mimicking biochar-albedo feedback in complex Mediterranean agricultural landscapes. *Environmental Research Letters* 2015, *10*, 084014, doi:10.1088/1748-9326/10/8/084014.
51. Haider, G.; Steffens, D.; Moser, G.; Müller, C.; Kammann, C.I. Biochar reduced nitrate leaching and improved soil moisture content without yield improvements in a four-year field study. *Agriculture, Ecosystems & Environment* 2017, *237*, 80-94, doi:https://doi.org/10.1016/j.agee.2016.12.019.

Preprints (www.preprints.org) | NOT PEER-REVIEWED | Posted: 9 April 2021 doi:10.20944/preprints202104.0267.v1

52. Agegnehu, G.; Bass, A.M.; Nelson, P.N.; Bird, M.I. Benefits of biochar, compost and biochar–compost for soil quality, maize yield and greenhouse gas emissions in a tropical agricultural soil. *Science of The Total Environment* 2016, *543*, 295-306, doi:https://doi.org/10.1016/j.scitotenv.2015.11.054.
53. Pallardy, S.G. Absorption of Water and Ascent of Sap. In *Physiology of Woody Plants*, Third Edition ed.; Pallardy, S.G., Ed.; Elsevier Inc: 2008; pp. 287-323.
54. Manzoni, S.; Vico, G.; Porporato, A.; Katul, G. Biological constraints on water transport in the soil–plant–atmosphere system. *Advances in Water Resources* 2013, *51*, 292-304, doi:https://doi.org/10.1016/j.advwatres.2012.03.016.
55. Lhomme, J.P.; Elguero, E. Examination of evaporative fraction diurnal behaviour using a soil-vegetation model coupled with a mixed-layer model. *Hydrol. Earth Syst. Sci.* 1999, *3*, 259-270, doi:10.5194/hess-3-259-1999.
56. Damm, A.; Paul-Limoges, E.; Haghighi, E.; Simmer, C.; Morsdorf, F.; Schneider, F.D.; van der Tol, C.; Migliavacca, M.; Rascher, U. Remote sensing of plant-water relations: An overview and future perspectives. *Journal of Plant Physiology* 2018, *227*, 3-19, doi:https://doi.org/10.1016/j.jplph.2018.04.012.